Supplementary Information

Adaptation of temperature optima of vegetation productivity across global biomes

Mengtian Huang, Shilong Piao*, Philippe Ciais, Josep Peñuelas, Xuhui Wang, Trevor F. Keenan, Shushi Peng, Joseph A. Berry, Kai Wang, Jiafu Mao, Ramdane Alkama, Alessandro Cescatti, Matthias Cuntz, Hannes De Deurwaerder, Mengdi Gao, Yue He, Yongwen Liu, Yiqi Luo, Ranga B. Myneni, Shuli Niu, Xiaoying Shi, Wenping Yuan, Hans Verbeeck, Tao Wang, Jin Wu, Ivan A. Janssens

* Correspondence to: slpiao@pku.edu.cn

Contents

Supplementary Figure 1.

The distribution of ecosystem-scale optimal temperature for vegetation productivity (T_{opt}^{eco}) derived from FLUXNET eddy covariance measurements across the globe. Climate zones are defined as tropical (20°S-20°N), temperate (20°N-50°N and 20°S-50°S) and boreal (north of 50°N) regions, respectively. Solid symbols indicate the average T_{opt}^{eco} value for each climate zone. Shaded area refers to the distribution of T_{opt}^{eco} values for each zone. The number of sites distributed in each climate zone is shown at the bottom.

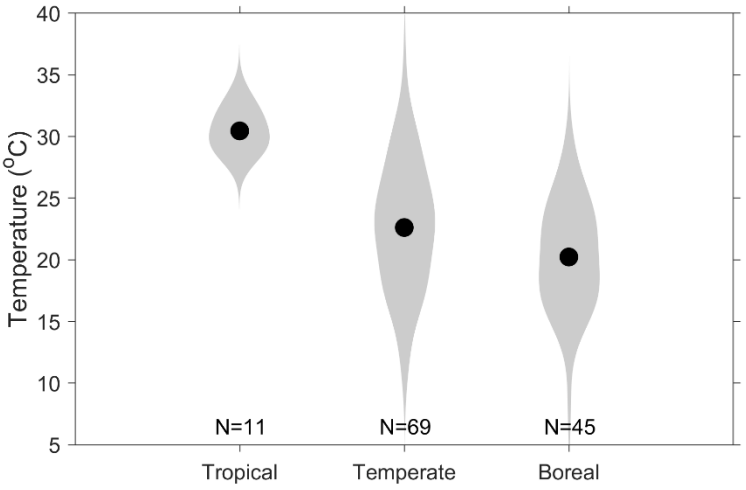

Supplementary Figure 2.

The ecosystem-scale optimal temperature for vegetation productivity (T_{opt}^{eco}) estimated from different climate datasets and different methods. a, T_{opt}^{eco} derived using MODIS NIR_V and WATCH Forcing Data Methodology to ERA-Interim (WFDEI) climate data. **b**, T_{opt}^{eco} derived using MODIS NIR_V, CRU/NCEP climate data and a nonlinear regression method.

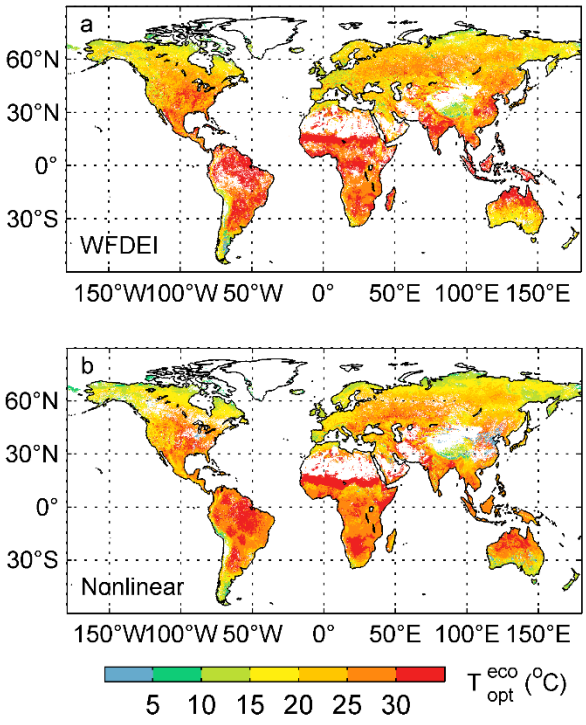

Supplementary Figure 3.

Relationship between ecosystem-scale optimal temperature of vegetation productivity (T_{opt}^{eco}) derived from MODIS near-infrared reflectance of terrestrial vegetation (MODIS NIRV) and from Normalized Difference Vegetation Index (NDVI) datasets. a, The spatial pattern of T_{opt}^{eco} derived from NDVI datasets was generated by averaging over estimates derived from the three NDVI datasets (GIMMS, MODIS and SPOT, respectively) using the same method as Fig. 1c. Given the inconsistent spatial resolutions of the different products, we resampled T_{opt}^{eco} to a common grid of 8 km before averaging. **b,** Scatter of T_{opt}^{eco} derived from NDVI datasets and those derived from MODIS NIRV. Each point indicates T_{opt}^{eco} in each 8 km×8 km window. For each point, the NDVI derived T_{opt}^{eco} value was estimated as the average of the T_{opt}^{eco} values of three different sensors, and the NIRV derived T_{opt}^{eco} value was estimated as the average of the T_{opt}^{eco} values in the 8 km×8 km pixel window. The dot line in gray represents y=x and the dot line in red is y=0.81x+3.08, which is derived by linear regression.

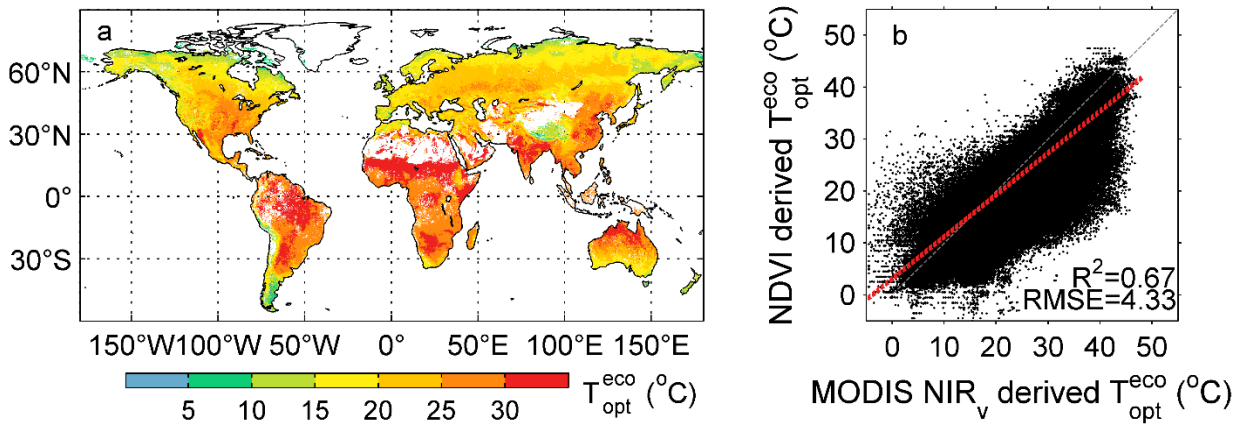

Supplementary Figure 4.

Relationship between ecosystem-scale optimal temperature of vegetation productivity (T_{opt}^{eco}) derived from MODIS near-infrared reflectance of terrestrial vegetation (MODIS NIRv) and from MODIS Enhanced Vegetation Index (EVI) data. a, The spatial pattern of T_{opt}^{eco} derived from EVI datasets using the same method as Fig. 1c. **b,** Scatter of T_{opt}^{eco} derived from NDVI datasets and those derived from EVI datasets. Each point indicates T_{opt}^{eco} in each 1 km×1 km pixel. The dot line in gray represents y=x and the dot line in red is y=0.98x+0.12, which is derived by linear regression.

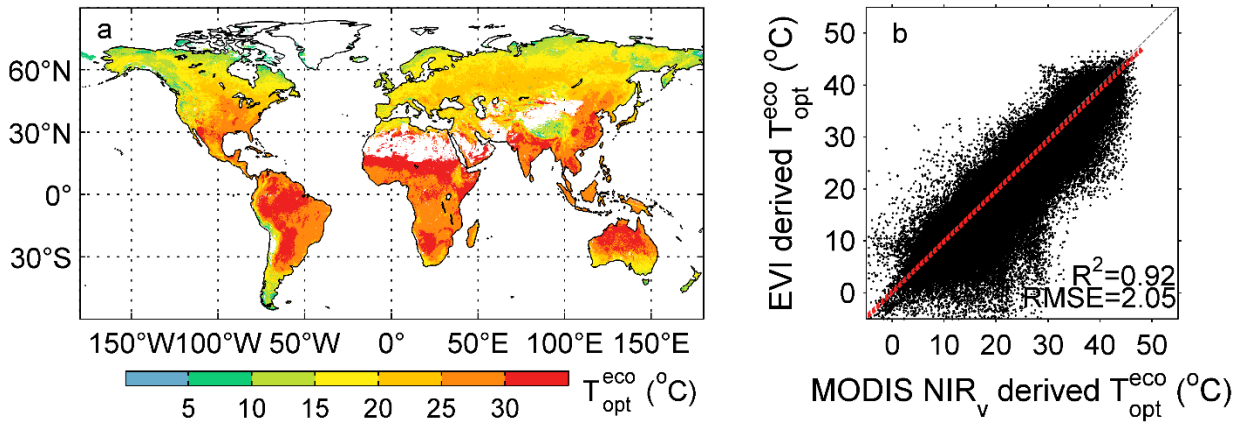

Supplementary Figure 5.

Relationship between ecosystem-scale optimal temperature for vegetation productivity (T_{opt}^{eco}) derived from MODIS near-infrared reflectance of terrestrial vegetation (MODIS NIRV) and from Sun-induced Chlorophyll Fluorescence (SIF) data. a, The spatial pattern of T_{opt}^{eco} derived from SIF using the same method as Fig. 1c. **b,** Scatter of T_{opt}^{eco} derived from NIR_V and those derived from SIF. Each point indicates T_{opt}^{eco} in each $2^o \times 2^o$ pixel. For each point, the NIR_V derived T_{opt}^{eco} value was estimated as the average of T_{opt}^{eco} values in the $2^o \times 2^o$ pixel window, and the fluorescence derived T_{opt}^{eco} as the average of four fluorescence data (derived from two different retrieval windows, 757nm and 771nm, as well as the two polarization states, S and P). The dot line in gray represents y=x and the dot line in red is y=1.09x-2.81, which is derived by linear regression.

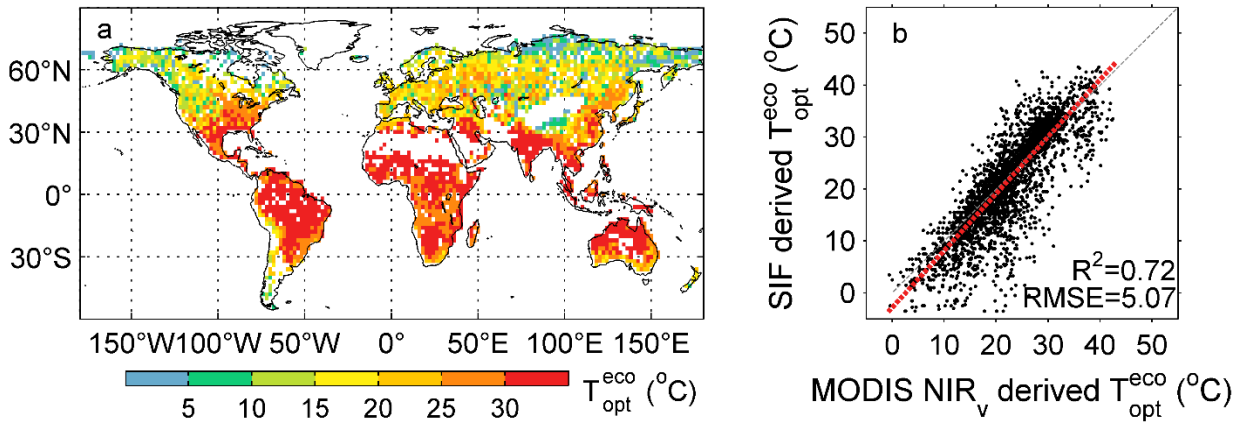

Supplementary Figure 6.

The ecosystem-scale optimal temperature for vegetation productivity (T_{opt}^{eco}) derived using the daily mean temperature (T_{mean}). a, The spatial pattern of T_{opt}^{eco} derived using T_{mean}. **b,** Scatter of T_{opt}^{eco} derived using the daily maximum temperature (T_{max}) and those derived using T_{mean}. The dot line in red represents y=x and the dot line in gray is y=0.90x-1.66, which is derived by linear regression.

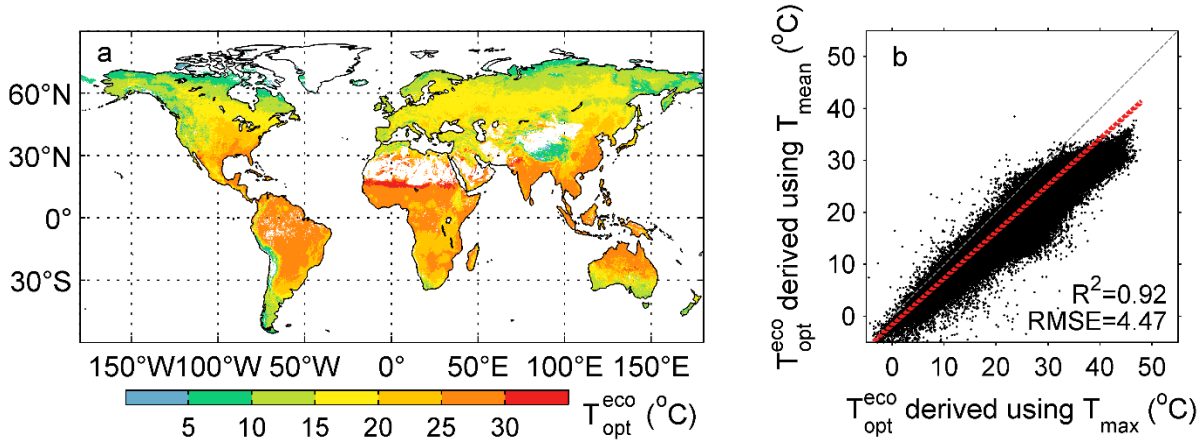

Supplementary Figure 7.

Comparison between the ecosystem-scale optimal temperature for vegetation productivity (T_{opt}^{eco}) estimated in this study and leaf-scale optimal temperature of V_{cmax} (T_{opt}^{leaf}) from leaf-scale measurements. T_{opt}^{eco} estimated in this study is determined using MODIS near-infrared reflectance of terrestrial vegetation (MODIS NIR_V) data.

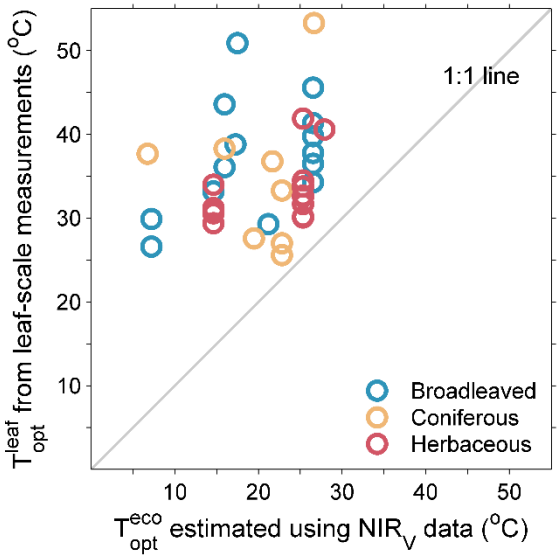

Supplementary Figure 8.

The distribution of optimal temperature for vegetation productivity (T_{opt}^{eco}) values and mean annual growing-season averaged daily maximum air temperature ($T_{max\ gs}^{air}$) values for different biomes across the globe. Solid symbols indicate the average T_{opt}^{eco} for each biome, and hollow symbols indicate the average $T_{max\ gs}^{air}$ for each biome. Shaded area with darker color refers to the distribution of T_{opt}^{eco} values for each biome, and that with lighter color refers to the distribution of $T_{max\ gs}^{air}$ values for the corresponding biome. The definition of each biome is the same as Fig. 2: ENF, evergreen needle-leaved forest; EBF, evergreen broad-leaved forest; DNF, deciduous needle-leaved forest; DBF, deciduous broad-leaved forest; MF, mixed forest; Shrub, closed shrublands and open shrublands**.**

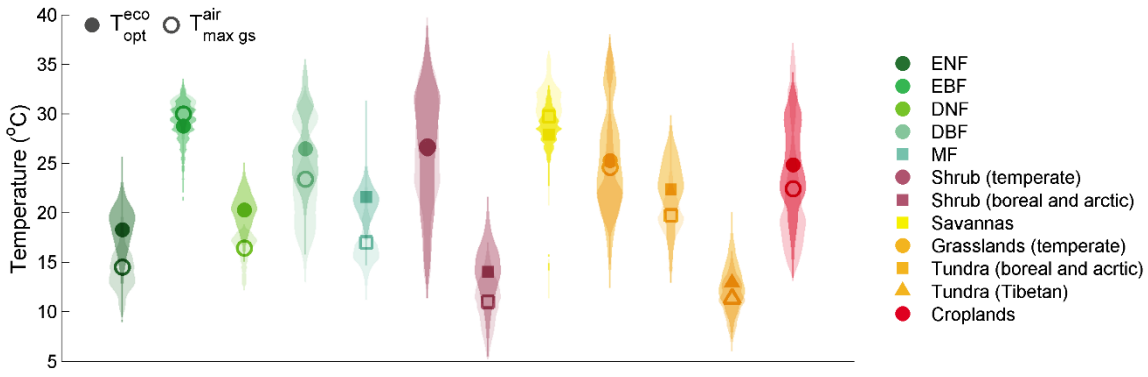

Supplementary Figure 9.

Differences between growing-season-averaged daily maximum air temperature ($T^{air}_{max\ gs}$) and ecosystem-scale optimal temperature for vegetation productivity (T^{eco}_{opt}) for different regions. Climate zones are defined as tropical (20°N-20°S), temperate (50°N-20°N and 20°S-50°S) and boreal (north of 50°N) regions, respectively. The future $T^{air}_{max\ gs}$ was calculated using IPCC predicted climate under three different RCP scenarios (RCP2.6, RCP4.5 and RCP8.5).

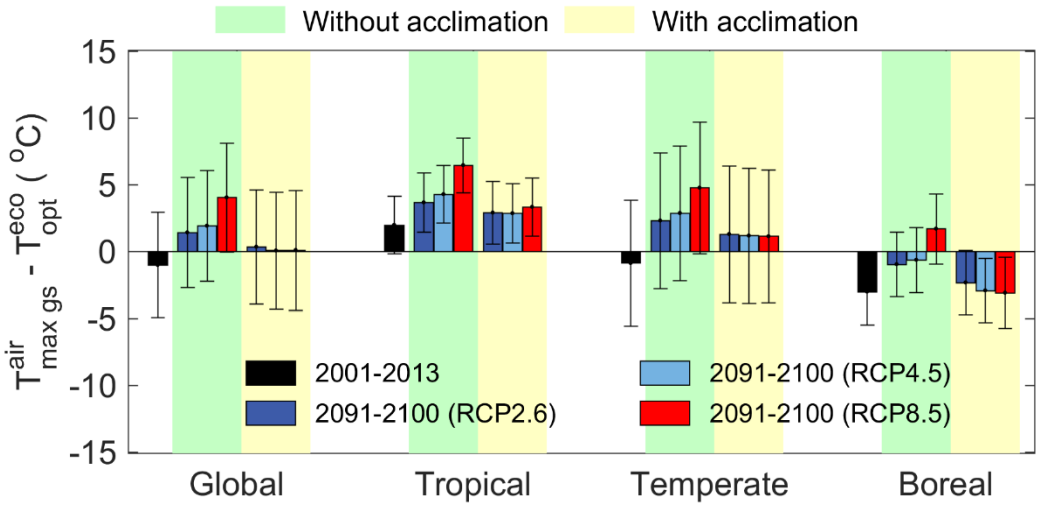

Supplementary Figure 10.

The percentiles in the biweekly averaged daily maximum air temperature (T_{max}) distribution when the ecosystem-scale optimal temperature for vegetation productivity (T_{opt}^{eco}) is observed.

T_{opt}^{eco} is determined based on MODIS near-infrared reflectance of terrestrial vegetation (MODIS NIR_V) data.

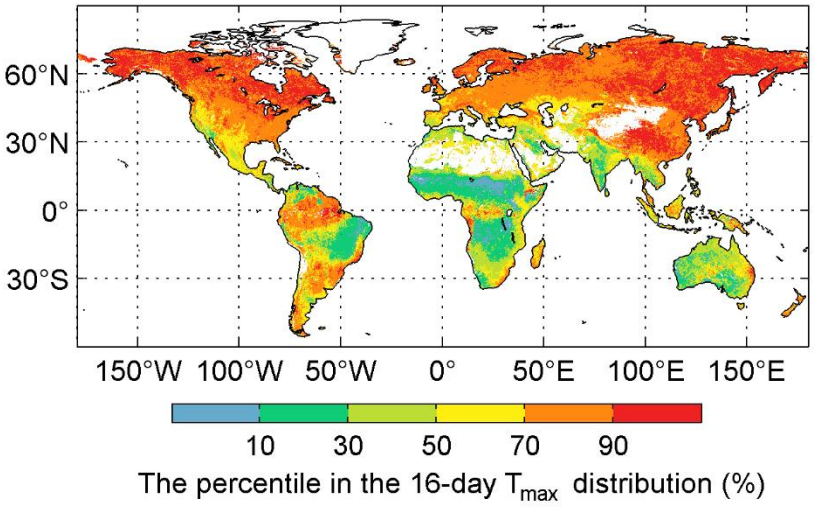

Supplementary Figure 11.

The ecosystem-scale optimal temperature for vegetation productivity (T_{opt}^{eco}) estimated from AVHRR NDVI datasets over three consecutive periods during 1982-2009. Spatial distribution of T_{opt}^{eco} over the period of 1982-1989 (**a**), 1990-1999 (**b**) and 2000-2009 (**c**), respectively. **d**, Latitudinal average T_{opt}^{eco} over the three periods. For each period, the solid line and shaded area indicate the mean and s.d. of T_{opt}^{eco} summarized by latitude.

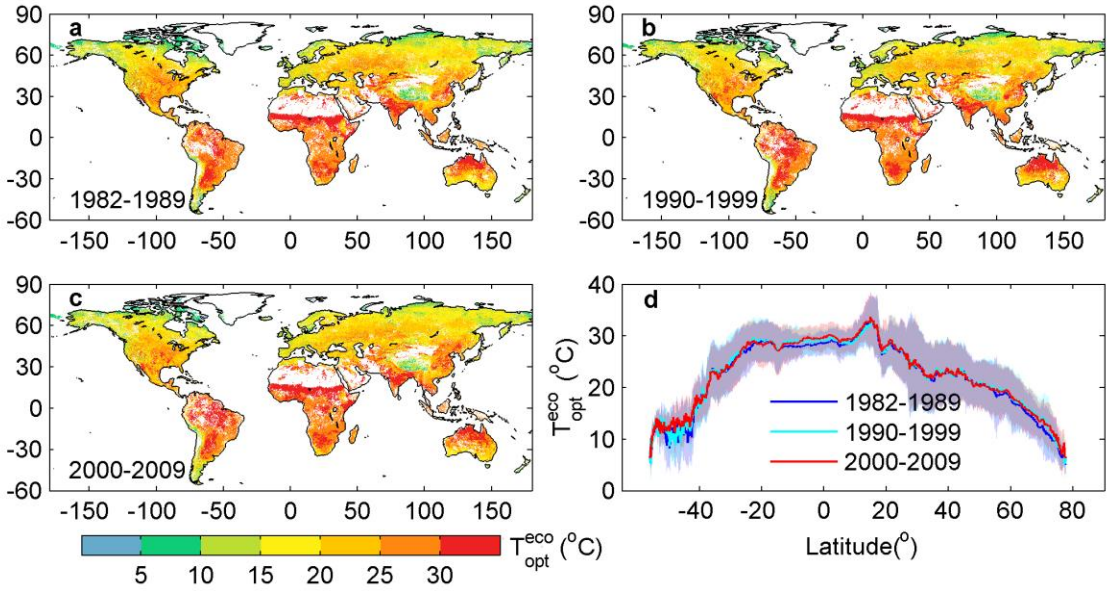

Supplementary Figure 12.

The relationship between the ecosystem-scale optimal temperature for Gross Primary Productivity (GPP) anomalies and the annual mean air temperature anomalies. Each point indicates a site-year. We used data from flux sites with more than 5 year GPP available and detectable T_{opt}^{eco} (see Methods).

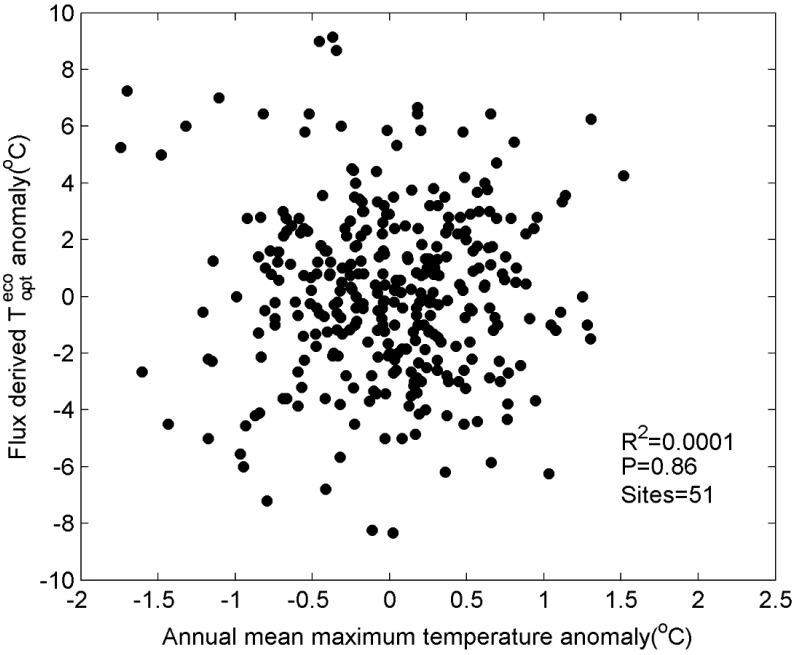

Supplementary Figure 13.

Change in ecosystem-scale optimal temperature for vegetation productivity (T_{opt}^{eco}) and growing-season-averaged daily maximum air temperature ($T_{max\ gs}^{air}$) across different latitudes. The upper charts current T_{opt}^{eco} versus future $T_{max\ gs}^{air}$ and the lower charts acclimated T_{opt}^{eco} versus future $T_{max\ gs}^{air}$. Current T_{opt}^{eco} and $T_{max\ gs}^{air}$ are calculated using current temperature during 2001-2013, whereas acclimated T_{opt}^{eco} and future $T_{max\ gs}^{air}$ are calculated using temperature during 2091-2100 projected from General Circulation Models (GCMs) under the RCP 2.6, 4.5 and 8.5 scenarios. Acclimated T_{opt}^{eco} is determined based on the projected temperature and temperature sensitivity of T_{opt}^{eco} given the annual precipitation level predicted for the period of 2091-2100. The solid line and shaded area in each panel indicate the mean and s.d. summarized by latitude.

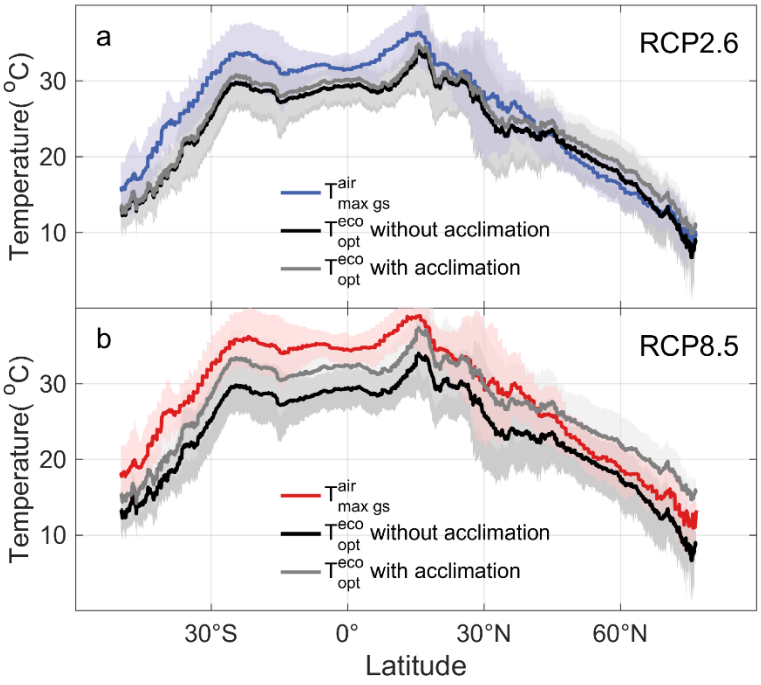

Supplementary Figure 14.

Change in optimal temperature for vegetation productivity (T_{opt}^{eco}) and growing-season-averaged daily maximum air temperature ($T_{max\ gs}^{air}$) for tropical evergreen forests. Future $T_{max\ gs}^{air}$ are calculated using temperature during 2091-2100 projected from 31 General Circulation Models (GCMs) under the RCP 2.6, 4.5 and 8.5 scenarios. Acclimated T_{opt}^{eco} is determined based on the projected temperature and temperature sensitivity of T_{opt}^{eco} given the current annual precipitation level, without considering precipitation shifts between the two periods. ** indicates that T_{opt}^{eco} is statistically significantly lower than $T_{max\ gs}^{air}$ at 99% (P<0.01) level based on Paired t-test.

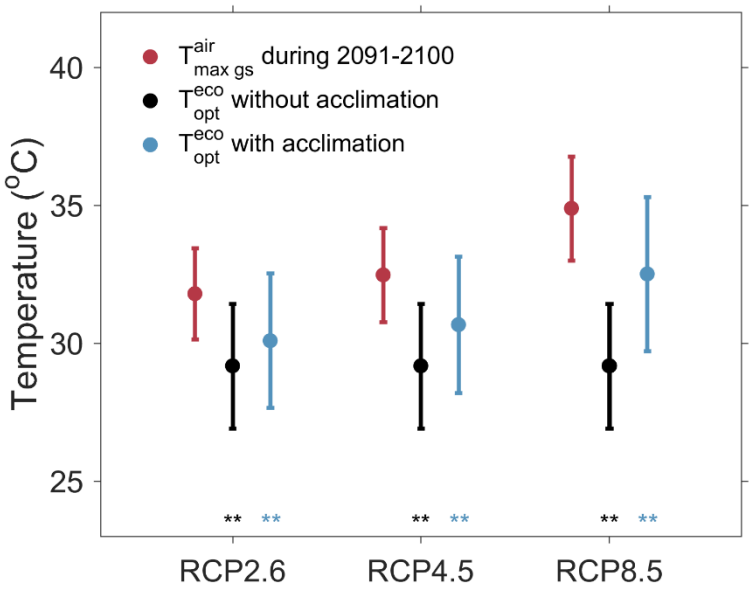

Supplementary Figure 15.

Comparisons between acclimated ecosystem-scale optimal temperature for vegetation productivity (T_{opt}^{eco}) and future growing-season-averaged daily maximum temperature ($T_{max\ gs}^{air}$). Acclimated T_{opt}^{eco} and future $T_{max\ gs}^{air}$ are calculated using temperature during 2091-2100 projected from 31 General Circulation Models (GCMs) under the RCP 2.6, 4.5 and 8.5 scenarios. Differently from Fig. 3, acclimated T_{opt}^{eco} is determined based on the projected temperature and temperature sensitivity of T_{opt}^{eco} given the current annual precipitation level, without considering precipitation shifts between the two periods. The solid line and shaded area indicated the mean and s.d. summarized by latitude.

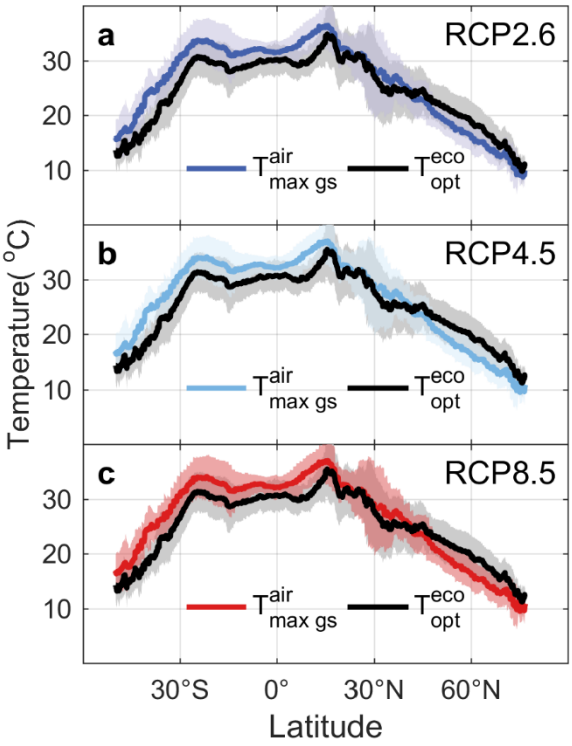

Supplementary Figure 16.

A case showing the use of temperature response curve to detect ecosystem-scale optimal temperature for vegetation productivity (T_{opt}^{eco}) for a pixel. Gray dots indicate the observed MODIS NIR_V and the corresponding 16-day-averaged air maximum temperature from 2001-2013, and black dots are the 90% quantile for each 1 ^oC temperature (see Methods).

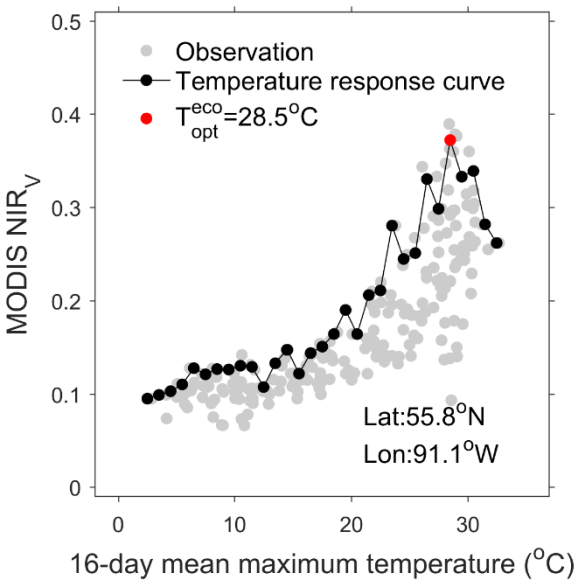

Supplementary Figure 17.

The ecosystem-scale optimal temperature for vegetation productivity (T_{opt}^{eco}) derived using MODIS near-infrared reflectance of terrestrial vegetation (MODIS NIRV) for different atmospheric vapor pressure deficit (VPD) bins. The spatial distribution of inferred T_{opt}^{eco} based on MODIS NIRV (**a**) is compared with that estimated using the same method but under the condition that VPD values fall in a specific range of 0-1 kPa (**b**), 1-2 kPa (**c**) and 2-3 kPa (**d**), respectively.

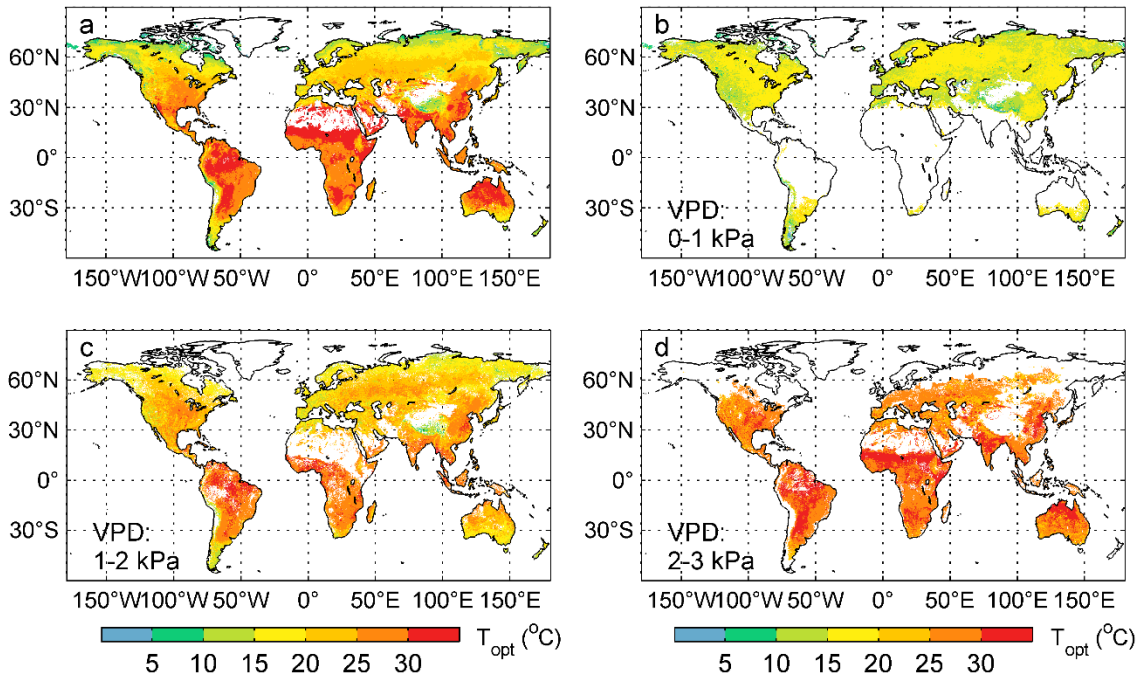

Supplementary Figure 18.

Variance inflation factor (VIF) between vapor pressure deficit (VPD) and $T_{\max gs}^{air}$ along the gradient of mean annual VPD. The variance inflation factor (VIF) between VPD and $T_{\max gs}^{air}$ under each VPD bin in the regression model shown in Eq.2 (see Methods).

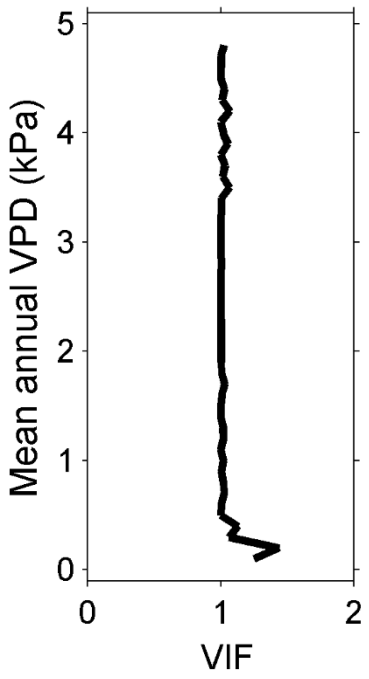

Supplementary Figure 19.

Apparent and partial temperature sensitivity of ecosystem-scale optimal temperature for vegetation productivity (T_{opt}^{eco}) along the gradient of mean annual vapor pressure deficit (VPD). The apparent sensitivity of T_{opt}^{eco} in response to changes in $T_{max\ gs}^{air}$ was calculated as the slope of the linear regression between T_{opt}^{eco} and $T_{max\ gs}^{air}$ for a given VPD level; the partial temperature sensitivity of T_{opt}^{eco} to $T_{max\ gs}^{air}$ was estimated based on a bilinear regression as a function of $T_{max\ gs}^{air}$ and VPD (see Methods). T_{opt}^{eco} is determined using NIR_V data from satellite observations from Moderate Resolution Imaging Spectroradiometer (MODIS).

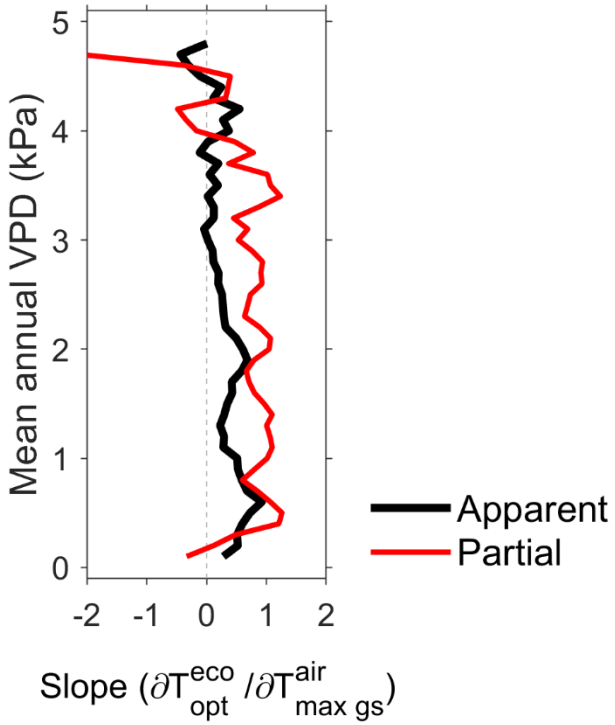

Supplementary Figure 20.

The percentiles of downward shortwave solar radiation (Rad) when the ecosystem-scale optimal temperature (T_{opt}^{eco}) is observed in the 16-day averaged Rad distribution. The 16-day averaged Rad data is derived from CRU/NCEP 6-hourly datasets. T_{opt}^{eco} is determined using MODIS NIR_V during 2001-2013.

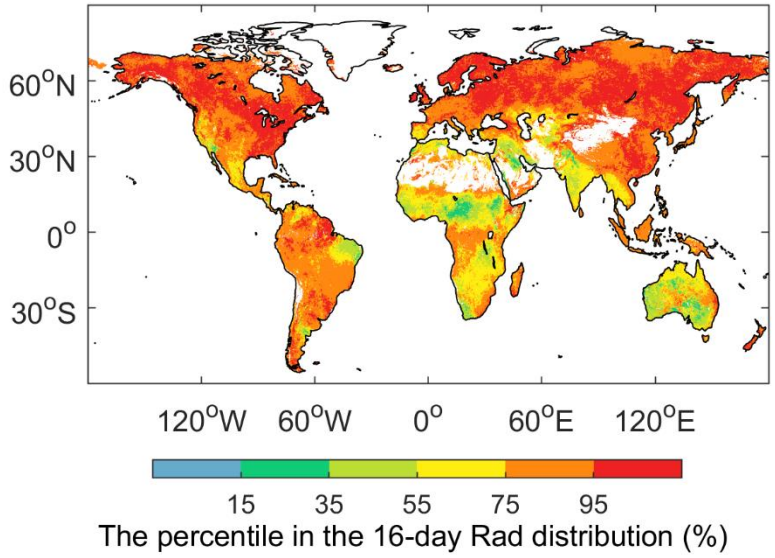

Supplementary Figure 21.

The ecosystem-scale optimal temperature for vegetation productivity (T_{opt}^{eco}) estimated from three different NDVI datasets. Spatial distribution of T_{opt}^{eco} is estimated using AVHRR (**a**), SPOT (**b**), and MODIS (**c**), respectively. **d**, Latitudinal average T_{opt}^{eco} estimated from different datasets. For each estimate, the solid line and shaded area indicate the mean and s.d. of T_{opt}^{eco} summarized by latitude.

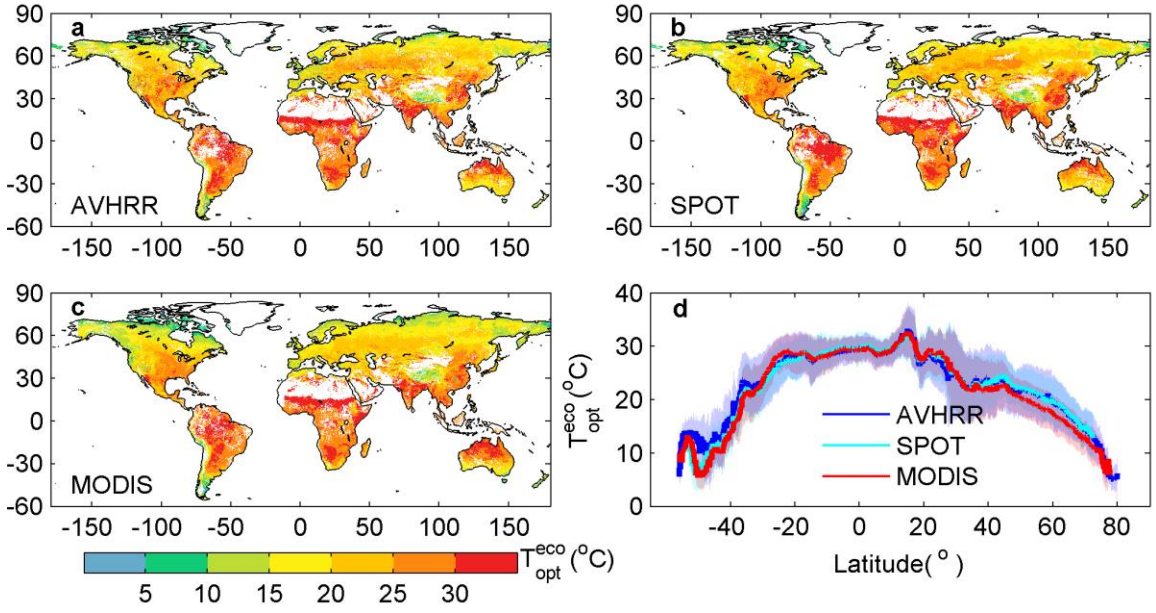

Supplementary Figure 22.

Ecosystem-scale optimal temperature of vegetation productivity (T_{opt}^{eco}) derived from MODIS near-infrared reflectance of vegetation (NIRv) using daily maximum land surface temperature ($T_{max}^{surface}$). $T_{max}^{surface}$ datasets were inferred from MODIS-Aqua with the overpass time of 1:30 P.M. (see Methods). Only pixels with annual mean NDVI value larger than 0.1 and detectable T_{opt}^{eco} are shown here.

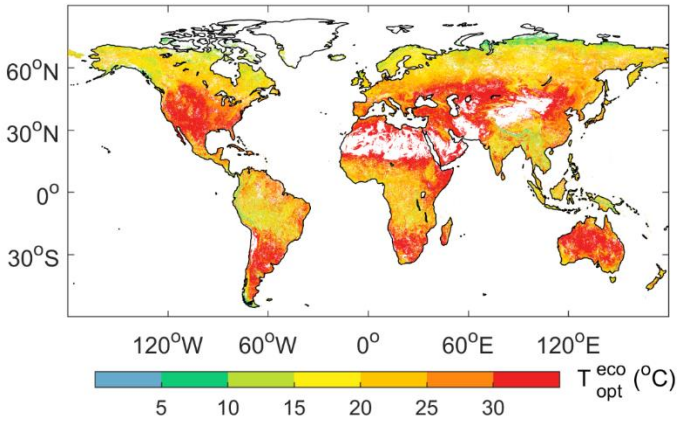

Supplementary Table 1.

The ecosystem-scale optimal temperature for vegetation productivity (T_{opt}^{eco}) derived from daily Gross Primary Productivity (GPP) and corresponding temperature measurements from eddy covariance sites. Data from all sites except for BR-Ban, BR-Cax, BR-Ji1, BR-Ji2, BR-Ma2, BR-Sa1, BR-Sa2, BR-Sp1 were gathered from www.fluxdata.org.

Site ID	Latitude	Longitude	T_{opt}^{eco} (ºC)	Reference
AT-Neu	47.1ºN	11.3ºE	23.5	74
AU-Fog	12.5ºS	131.3ºE	29.5	--
AU-How	12.5ºS	131.2ºE	31.2	75
AU-Tum	35.7ºS	148.2ºE	26.1	76
AU-Wac	37.4ºS	145.2ºE	25.5	--
BE-Bra	51.3ºN	4.5ºE	23.2	77
BE-Jal	50.6ºN	6.1ºE	28.5	--
BE-Lon	50.6ºN	4.7ºE	26.0	77
BE-Vie	50.3ºN	6ºE	24.2	79
BR-Ban	9.8ºS	50.2ºW	29.5	--
BR-Cax	1.7ºS	51.5ºW	32.5	--
BR-Ji1	10.8ºS	62.4ºW	31.5	--
BR-Ji2	10.1ºS	61.9ºW	31.5	--
BR-Ma2	2.6ºS	60.2ºW	29.5	--
BR-Sa1	2.9ºS	55ºW	33.5	--
BR-Sa2	3ºS	54.5ºW	28.5	--
BR-Sp1	21.6ºS	47.6ºW	28.5	--
BW-Ma1	19.9ºS	23.6ºE	29.8	80
CA-Man	55.9ºN	98.5ºW	17.3	81
CA-Mer	45.4ºN	75.5ºW	25.8	82
CA-NS1	55.9ºN	98.5ºW	16.5	83
CA-NS2	55.9ºN	98.5ºW	8.2	83
CA-NS3	55.9ºN	98.4ºW	18.2	83
CA-NS4	55.9ºN	98.4ºW	17.5	83
CA-NS5	55.9ºN	98.5ºW	22.5	83

Site ID	Latitude	Longitude	T_{opt}^{eco} (°C)	Reference
CA-NS6	55.9°N	99°W	21.5	83
CA-NS7	56.6°N	99.9°W	19.5	83
CA-Qcu	49.3°N	74°W	17.5	84
CA-Qfo	49.7°N	74.3°W	17.2	84
CH-Oe1	47.3°N	7.7°E	22.3	85
CH-Oe2	47.3°N	7.7°E	16.5	85
CZ-BK1	49.5°N	18.5°E	23.5	86
DE-Bay	50.1°N	11.9°E	23.8	87
DE-Geb	51.1°N	10.9°E	16.5	88
DE-Gri	50.9°N	13.5°E	23.0	89
DE-Hai	51.1°N	10.5°E	23.8	90
DE-Kli	50.9°N	13.5°E	29.0	91
DE-Meh	51.3°N	10.7°E	23.0	92
DE-Tha	51°N	13.6°E	23.7	93
DE-Wet	50.5°N	11.5°E	20.1	94
DK-Lva	55.7°N	12.1°E	15.5	89
DK-Ris	55.5°N	12.1°E	17.5	91
DK-Sor	55.5°N	11.6°E	21.7	95
ES-ES1	39.3°N	0.3°W	22.5	86
ES-ES2	39.3°N	0.3°W	30.5	88
ES-LMa	39.9°N	5.8°W	18.8	96
ES-VDA	42.2°N	1.4°E	17.8	97
FI-Hyy	61.8°N	24.3°E	21.8	98
FI-Kaa	69.1°N	27.3°E	16.9	--
FI-Sod	67.4°N	26.6°E	16.1	98
FR-Fon	48.5°N	2.8°E	26.0	97
FR-Gri	48.8°N	2°E	18.5	97
FR-Hes	48.7°N	7.1°E	24.3	99
FR-Lam	43.5°N	1.2°E	18.5	--
FR-LBr	44.7°N	0.8°W	25.0	100

Site ID	Latitude	Longitude	T_{opt}^{eco} (°C)	Reference
FR-Lq1	45.6°N	2.7°E	22.8	89
FR-Lq2	45.6°N	2.7°E	21.5	89
FR-Pue	43.7°N	3.6°E	17.0	101
HU-Bug	46.7°N	19.6°E	25.5	--
HU-Mat	47.8°N	19.7°E	21.5	102
ID-Pag	2.3°N	114°E	28.0	103
IE-Ca1	52.9°N	6.9°W	16.2	89
IE-Dri	52°N	8.8°W	16.5	104
IL-Yat	31.3°N	35.1°E	23.7	--
IT-Amp	41.9°N	13.6°E	16.8	89
IT-BCi	40.5°N	15°E	27.5	97
IT-Col	41.8°N	13.6°E	20.7	105
IT-Cpz	41.7°N	12.4°E	22.8	106
IT-Lav	46°N	11.3°E	17.5	107
IT-Lec	43.3°N	11.3°E	13.5	108
IT-LMa	45.6°N	7.2°E	12.0	--
IT-Mal	46.1°N	11.7°E	11.0	89
IT-MBo	46°N	11°E	17.5	109
IT-Non	44.7°N	11.1°E	22.8	86
IT-PT1	45.2°N	9.1°E	23.5	109
IT-Ren	46.6°N	11.4°E	13.5	109
IT-Ro1	42.4°N	11.9°E	19.2	110
IT-Ro2	42.4°N	11.9°E	19.9	111
IT-SRo	43.7°N	10.3°E	16.6	112
NL-Ca1	52°N	4.9°E	21.8	89
NL-Hor	52°N	5.1°E	25.5	113
NL-Lan	52°N	4.9°E	23.5	--
NL-Loo	52.2°N	5.7°E	20.6	114
PL-wet	52.8°N	16.3°E	24.5	115
PT-Esp	38.6°N	8.6°W	19.8	--

Site ID	Latitude	Longitude	T_{opt}^{eco} (°C)	Reference
PT-Mi1	38.5°N	8°W	20.5	116
PT-Mi2	38.5°N	8°W	19.5	96
RU-Fyo	56.5°N	32.9°E	24.4	117
RU-Ha1	54.7°N	90°E	26.5	118
SE-Deg	64.2°N	19.5°E	18.5	118
SE-Fla	64.1°N	19.5°E	15.3	118
SE-Nor	60.1°N	17.5°E	18.5	--
SE-Sk1	60.1°N	17.9°E	16.5	--
SE-Sk2	60.1°N	17.8°E	16.5	--
UK-EBu	55.9°N	3.2°W	19.5	96
UK-ESa	55.9°N	2.9°W	17.5	108
UK-Gri	56.6°N	3.8°W	13.7	120
UK-Ham	51.2°N	0.9°W	19.0	--
UK-PL3	51.5°N	1.3°W	20.5	--
US-ARM	36.6°N	97.5°W	22.0	121
US-Aud	31.6°N	110.5°W	35.8	96
US-Bar	44.1°N	71.3°W	23.0	122
US-Bkg	44.3°N	96.8°W	25.0	123
US-Blo	38.9°N	120.6°W	24.4	124
US-Bo1	40°N	88.3°W	23.1	97
US-FPe	48.3°N	105.1°W	16.5	96
US-Goo	34.3°N	89.9°W	29.3	96
US-Ha1	42.5°N	72.2°W	24.3	125
US-Ho1	45.2°N	68.7°W	22.9	126
US-Ho2	45.2°N	68.7°W	22.3	127
US-Me4	44.5°N	121.6°W	17.5	128
US-MMS	39.3°N	86.4°W	29.9	129
US-MOz	38.7°N	92.2°W	27.5	130
US-Ne1	41.2°N	96.5°W	31.2	131
US-Ne2	41.2°N	96.5°W	30.5	131

Site ID	Latitude	Longitude	T_{opt}^{eco} (°C)	Reference
US-Ne3	41.2°N	96.4°W	29.2	131
US-Oho	41.6°N	83.8°W	30.0	132
US-PFa	45.9°N	90.3°W	21.7	133
US-SP2	29.8°N	82.2°W	26.5	97
US-SP3	29.8°N	82.2°W	28.0	97
US-Syv	46.2°N	89.3°W	26.8	134
US-Ton	38.4°N	121°W	18.5	135
US-Var	38.4°N	121°W	17.7	135
US-WBW	36°N	84.3°W	27.1	--
US-WCr	45.8°N	90.1°W	22.8	137
ZA-Kru	25°S	31.5°E	31.0	138

Supplementary Table 2.

List of models that participated in the phase five of Coupled Model Intercomparison Project (CMIP5) used in this study.

	Model Name	RCP2.6	RCP4.5	RCP8.5
1	ACCESS1-0			√
2	ACCESS1-3			√
3	BNU-ESM	√	√	
4	CMCC-CESM			√
5	CMCC-CM		√	
6	CMCC-CMS		√	
7	CNRM-CM5	√	√	
8	CSIRO-Mk3-6-0	√	√	
9	CanESM2	√	√	√
10	EC-EARTH		√	√
11	FGOALS-g2	√	√	√
12	IPSL-CM5A-MR	√		√
13	MIROC-ESM	√		√
14	MIROC5	√		√
15	MPI-ESM-LR	√	√	
16	MPI-ESM-MR	√	√	√
17	MRI-CGCM3	√	√	
18	NorESM1-M	√		
19	bcc-csm1-1	√	√	√
20	inmcm4		√	

Supplementary References

74. Wohlfahrt, G. *et al.* Seasonal and inter-annual variability of the net ecosystem CO_2 exchange of a temperate mountain grassland: Effects of weather and management. *Journal of Geophysical Research: Atmospheres* **113**, D08110, doi:10.1029/2007JD009286 (2008).
75. Eamus, D., Hutley, L. B., O'Grady, A. P. Daily and seasonal patterns of carbon and water fluxes above a north Australian savanna. *Tree Physiology* **21**, 977-988 (2001).
76. van Gorsel, E. *et al.* Application of an alternative method to derive reliable estimates of nighttime respiration from eddy covariance measurements in moderately complex topography. *Agricultural and Forest Meteorology* **148**, 1174-1180 (2008).
77. Gielen, B., Verbeeck, H., Neirynck, J., Vermeiren, F., Janssens, I. A. Decadal water balance of a temperate Scots pine forest (*Pinus sylvestris L.*) based on measurements and modelling. *Biogeosciences* **7**, 1247-1261 (2010).
78. Moureaux, C., Debacq, A., Bodson, B., Heinesch, B., Aubinet, M. Annual net ecosystem carbon exchange by a sugar beet crop. *Agricultural and Forest Meteorology* **139**, 25-39 (2006).
79. Aubinet, M. *et al.* Long term carbon dioxide exchange above a mixed forest in the Belgian Ardennes. *Agricultural and Forest Meteorology* **108**, 293-315 (2001).
80. Veenendaal, E. M., Kolle, O., Lloyd, J. Seasonal variation in energy fluxes and carbon dioxide exchange for a broad-leaved semi-arid savanna (Mopane woodland) in Southern Africa. *Global Change Biology* **10**, 318-328 (2004).
81. Dunn, A. L., Barford, C. C., Wofsy, S. C., Goulden, M. L., Daube, B. C. A long-term record of carbon exchange in a boreal black spruce forest: Means, responses to interannual variability, and decadal trends. *Global Change Biology* **13**, 577-590 (2007).
82. Lafleur, P. M., Roulet, N. T., Bubier, J. L., Frolking, S., Moore, T. R. Interannual variability in the peatland-atmosphere carbon dioxide exchange at an ombrotrophic bog. *Global Biogeochemical Cycles* **17**, 1036 (2003).
83. Goulden, M. L., Miller, S. D., Da Rocha, H. R. Nocturnal cold air drainage and pooling in a tropical forest. *Journal of Geophysical Research: Atmospheres* **111**, D08S04, doi:10.1029/2005JD006037 (2006).
84. Giasson, M. A., Coursolle, C., Margolis, H. A. Ecosystem-level CO_2 fluxes from a boreal cutover in eastern Canada before and after scarification. *Agricultural and Forest Meteorology* **140**, 23-40 (2006).

85. Ammann, C., Flechard, C., Leifeld, J., Neftel, A., Fuhrer, J. The carbon budget of newly established temperate grassland depends on management intensity. *Agriculture, Ecosystems & Environment* **121**, 5-20 (2007).
86. Reichstein, M. *et al.* On the separation of net ecosystem exchange into assimilation and ecosystem respiration: review and improved algorithm. *Global Change Biology* **11**, 1424-1439 (2005).
87. Valentini, R. *et al.* Respiration as the main determinant of carbon balance in European forests. *Nature* **404**, 861 (2000).
88. Anthoni, P. *et al.* Forest and agricultural land-use-dependent CO_2 exchange in Thuringia, Germany. *Global Change Biology* **10**, 2005-2019 (2004).
89. Gilmanov, T. *et al.* Partitioning European grassland net ecosystem CO_2 exchange into gross primary productivity and ecosystem respiration using light response function analysis. *Agriculture, ecosystems & environment* **121**, 93-120 (2007).
90. Knohl, A., Schulze, E. D., Kolle, O., Buchmann, N. Large carbon uptake by an unmanaged 250-year-old deciduous forest in Central Germany. *Agricultural and Forest Meteorology* **118**, 151-167 (2003).
91. Chen, B. *et al.* A data-model fusion approach for upscaling gross ecosystem productivity to the landscape scale based on remote sensing and flux footprint modelling. *Biogeosciences* **7**, 2943-2958 (2010).
92. Don, A., Rebmann, C., Kolle, O., Scherer-Lorenzen, M., Schulze, E. D. Impact of afforestation-associated management changes on the carbon balance of grassland. *Global Change Biology* **15**, 1990-2002 (2009).
93. Arain, M. A., Restrepo-Coupe, N. Net ecosystem production in a temperate pine plantation in southeastern Canada. *Agricultural and Forest Meteorology* **128**, 223-241 (2005).
94. Rebmann, C. *et al.* Treatment and assessment of the CO_2-exchange at a complex forest site in Thuringia, Germany. *Agricultural and Forest Meteorology* **150**, 684-691 (2010).
95. Pilegaard, K. *et al.* Field measurements of atmosphere-biosphere interactions in a Danish beech forest. *Boreal Environment Research* **8**, 315-334 (2003).
96. Yi, C. *et al.* Climate control of terrestrial carbon exchange across biomes and continents. *Environmental Research Letters* **5**, 034007 (2010).

97. Migliavacca, M. *et al.* Semiempirical modeling of abiotic and biotic factors controlling ecosystem respiration across eddy covariance sites. *Global Change Biology* **17**, 390-409 (2011).
98. Suni, T. *et al.* Long-term measurements of surface fluxes above a Scots pine forest in Hyytiala, southern Finland, 1996-2001. *Boreal Environment Research* **8**, 287-302 (2003).
99. Granier, A. *et al.* The carbon balance of a young beech forest. *Functional ecology* **14**, 312-325 (2000).
100. Berbigier, P., Bonnefond, J.M., Mellmann, P. CO_2 and water vapour fluxes for 2 years above Euroflux forest site. *Agricultural and Forest Meteorology* **108**, 183-197 (2001).
101. Rambal, S., Joffre, R., Ourcival, J., Cavender-Bares, J., Rocheteau, A. The growth respiration component in eddy CO_2 flux from a Quercus ilex mediterranean forest. *Global Change Biology* **10**, 1460-1469 (2004).
102. Pintér, K. *et al.* Interannual variability of grasslands' carbon balance depends on soil type. *Community Ecology* **9**, 43-48 (2008).
103. Hirano, T. *et al.* Carbon dioxide balance of a tropical peat swamp forest in Kalimantan, Indonesia. *Global Change Biology* **13**, 412-425 (2007).
104. Jaksic, V. *et al.* Net ecosystem exchange of grassland in contrasting wet and dry years. *Agricultural and Forest Meteorology* **139**, 323-334 (2006).
105. Van Dijk, A. I., Dolman, A., Estimates of CO_2 uptake and release among European forests based on eddy covariance data. *Global Change Biology* **10**, 1445-1459 (2004).
106. Garbulsky, M. F., Peñuelas, J., Papale, D., Filella, I. Remote estimation of carbon dioxide uptake by a Mediterranean forest. *Global Change Biology* **14**, 2860-2867 (2008).
107. Marcolla, B., Pitacco, A., Cescatti, A. Canopy architecture and turbulence structure in a coniferous forest. *Boundary-layer meteorology* **108**, 39-59 (2003).
108. Groenendijk, M. *et al.* Assessing parameter variability in a photosynthesis model within and between plant functional types using global Fluxnet eddy covariance data. *Agricultural and Forest Meteorology* **151**, 22-38 (2011).
109. Migliavacca, M. *et al.* Modeling gross primary production of agro-forestry ecosystems by assimilation of satellite-derived information in a process-based model. *Sensors* **9**, 922-942 (2009).

110. Rey, A. *et al.* Annual variation in soil respiration and its components in a coppice oak forest in Central Italy. *Global Change Biology* **8**, 851-866 (2002).
111. Tedeschi, V. *et al.* Soil respiration in a Mediterranean oak forest at different developmental stages after coppicing. *Global Change Biology* **12**, 110-121 (2006).
112. Chiesi, M. *et al.* Modelling carbon budget of Mediterranean forests using ground and remote sensing measurements. *Agricultural and Forest Meteorology* **135**, 22-34 (2005).
113. Jacobs, C. *et al.* Variability of annual CO_2 exchange from Dutch grasslands. *Biogeosciences* **4**, 803-816 (2007).
114. Dolman, A., Moors, E., Elbers, J. The carbon uptake of a mid latitude pine forest growing on sandy soil. *Agricultural and Forest Meteorology* **111**, 157-170 (2002).
115. Chojnicki, B. H., Urbaniak, M., Józefczyk, D., Augustin, J., Olejnik, J. Measurements of gas and heat fluxes at Rzecin wetland. *Wetlands: monitoring, modeling and management (Okruszko, ed). Taylor & Francis Group, London: pp*, 125-131 (2007).
116. Reichstein, M. *et al.* Modeling temporal and large-scale spatial variability of soil respiration from soil water availability, temperature and vegetation productivity indices. *Global biogeochemical cycles* **17**, 1104 (2003).
117. Kurbatova, J., Li, C., Varlagin, A., Xiao, X., Vygodskaya, N. Modeling carbon dynamics in two adjacent spruce forests with different soil conditions in Russia. *Biogeosciences* **5**, 969-980 (2008).
118. Chevallier, F., Viovy, N., Reichstein, M., Ciais, P. On the assignment of prior errors in Bayesian inversions of CO_2 surface fluxes. *Geophysical Research Letters* **33**, L13802 (2006).
119. Lindroth, A., Klemedtsson, L., Grelle, A., Weslien, P., Langvall, O. Measurement of net ecosystem exchange, productivity and respiration in three spruce forests in Sweden shows unexpectedly large soil carbon losses. *Biogeochemistry* **89**, 43-60 (2008).
120. Rebmann, C. *et al.* Quality analysis applied on eddy covariance measurements at complex forest sites using footprint modelling. *Theoretical and Applied Climatology* **80**, 121-141 (2005).
121. Fischer, M. L., Billesbach, D. P., Berry, J. A., Riley, W. J., Torn, M. S. Spatiotemporal variations in growing season exchanges of CO_2, H_2O, and sensible heat in agricultural fields of the Southern Great Plains. *Earth Interactions* **11**, 1-21 (2007).

122. Jenkins, J. *et al.* Refining light-use efficiency calculations for a deciduous forest canopy using simultaneous tower-based carbon flux and radiometric measurements. *Agricultural and Forest Meteorology* **143**, 64-79 (2007).

123. Gilmanov, T. G. *et al.* Integration of CO_2 flux and remotely-sensed data for primary production and ecosystem respiration analyses in the Northern Great Plains: Potential for quantitative spatial extrapolation. *Global Ecology and Biogeography* **14**, 271-292 (2005).

124. Goldstein, A. *et al.* Effects of climate variability on the carbon dioxide, water, and sensible heat fluxes above a ponderosa pine plantation in the Sierra Nevada (CA). *Agricultural and Forest Meteorology* **101**, 113-129 (2000).

125. Urbanski, S. *et al.* Factors controlling CO_2 exchange on timescales from hourly to decadal at Harvard Forest. *Journal of Geophysical Research: Biogeosciences* **112**, G02020, doi:10.1029/2006JG000293 (2007).

126. Hollinger, D. *et al.* Spatial and temporal variability in forest-atmosphere CO_2 exchange. *Global Change Biology* **10**, 1689-1706 (2004).

127. Oren, R. *et al.* Estimating the uncertainty in annual net ecosystem carbon exchange: Spatial variation in turbulent fluxes and sampling errors in eddy-covariance measurements. *Global Change Biology* **12**, 883-896 (2006).

128. Sun, O. J., Campbell, J., Law, B. E., Wolf, V. Dynamics of carbon stocks in soils and detritus across chronosequences of different forest types in the Pacific Northwest, USA. *Global Change Biology* **10**, 1470-1481 (2004).

129. Schmid, H. P., Grimmond, C. S. B., Cropley, F., Offerle, B., Su, H.B. Measurements of CO_2 and energy fluxes over a mixed hardwood forest in the mid-western United States. *Agricultural and Forest Meteorology* **103**, 357-374 (2000).

130. Gu, Y. *et al.* Climatic effects of different aerosol types in China simulated by the UCLA general circulation model. *Journal of Geophysical Research: Atmospheres* **111**, D15201, doi 10.1029/2005jd006312 (2006).

131. Richardson, A. D. *et al.* A multi-site analysis of random error in tower-based measurements of carbon and energy fluxes. *Agricultural and Forest Meteorology* **136**, 1-18 (2006).

132. DeForest, J. L. *et al.* Phenophases alter the soil respiration–temperature relationship in an oak-dominated forest. *International Journal of Biometeorology* **51**, 135-144 (2006).

133. Davis, K. J. *et al.* The annual cycles of CO_2 and H_2O exchange over a northern mixed forest as observed from a very tall tower. *Global Change Biology* **9**, 1278-1293 (2003).
134. Desai, A. R., Bolstad, P. V., Cook, B. D., Davis, K. J., Carey, E. V. Comparing net ecosystem exchange of carbon dioxide between an old-growth and mature forest in the upper Midwest, USA. *Agricultural and Forest Meteorology* **128**, 33-55 (2005).
135. Ma, S., Baldocchi, D. D., Xu, L., Hehn, T. Inter-annual variability in carbon dioxide exchange of an oak/grass savanna and open grassland in California. *Agricultural and Forest Meteorology* **147**, 157-171 (2007).
136. Xu, L., Baldocchi, D. D. Seasonal variation in carbon dioxide exchange over a Mediterranean annual grassland in California. *Agricultural and Forest Meteorology* **123**, 79-96 (2004).
137. Cook, B. D. *et al.* Carbon exchange and venting anomalies in an upland deciduous forest in northern Wisconsin, USA. *Agricultural and Forest Meteorology* **126**, 271-295 (2004).
138. Williams, C. A., Hanan, N., Scholes, R. J., Kutsch, W. Complexity in water and carbon dioxide fluxes following rain pulses in an African savanna. *Oecologia* **161**, 469-480 (2009).